Formation and evolution of the solid electrolyte interphase on silicon electrodes from fluorine-free electrolytes

Zijie Lu, Tamara Patranika, Andrew J Naylor, Jonas Mindemark, Samuel Tardif, Guiomar Hernández, Sandrine Lyonnard

RESEARCH ARTICLE

NANO · MICRO small
www.small-journal.com

Formation and Evolution of the Solid Electrolyte Interphase on Silicon Electrodes from Fluorine-Free Electrolytes

Zijie Lu, Tamara Patranika, Andrew J. Naylor, Jonas Mindemark, Samuel Tardif, Guiomar Hernández,* and Sandrine Lyonnard**

With the increasing attention to energy storage solutions, a growing emphasis has been placed on environmentally compatible electrolytes tailored for lithium-ion batteries. This study investigates the surface behavior of Si wafers as model systems cycled with a fluorine-free electrolyte based on lithium bis(oxalato)borate (LiBOB), with and without the additive vinylene carbonate (VC). By utilizing *operando* X-ray reflectivity (XRR) and ex situ X-ray photoelectron spectroscopy (XPS), the intricate processes involved in solid electrolyte interphase (SEI) formation is elucidated, SiO_2/Si (de)lithiation, and the impact of the VC additive. Three distinct stages in SEI evolution during lithiation and delithiation are identified: SEI formation, subsequent densification and growth, and decrease in SEI thickness during delithiation, which collectively demonstrate the breathing behavior of the SEI during cycling. The addition of VC is found to mitigate LiBOB decomposition during cycling and promote a smoother SEI layer. Moreover, lithium trapping within the Si wafer post-delithiation is observed for both electrolytes but to a lesser extent with the addition of VC. This study offers structural and chemical insights into the fundamental processes governing SEI formation and Si wafer (de)lithiation in LiBOB-based electrolytes, with implications for designing environmentally friendly lithium-ion batteries.

1. Introduction

The increasing production of lithium-ion batteries (LIBs) to meet the growing demand for energy storage in electric vehicles, portable electronics, and the electricity grid emphasizes the need for safe, sustainable, and environmentally friendly battery technologies. In this regard, there is much emphasis on replacing electrode active materials and improving the production process; however, the electrolyte is often left behind and its main components have remained the same since the initial commercialization of LIBs. This electrolyte is composed of a fluorinated salt, lithium hexafluorophosphate ($LiPF_6$), dissolved in a mixture of carbonate solvents with many different additives, some of them fluorinated as well. Although a highly fluorinated electrolyte is considered a requirement for high performance,[1] it poses significant challenges to the sustainability and environmental impact of batteries.[2] $LiPF_6$ is prone to defluorination reactions resulting in toxic and corrosive compounds, such as HF and PF_5, which may result in detrimental reactions with other cell components.[3–5] Furthermore, they pose problems for the recycling of such batteries as their toxicity remains a safety hazard, they can corrode the reactors during recycling and fluorine remains easily as impurity in the recycled materials.[6–8] Additionally, the poor thermal stability of $LiPF_6$ leads to rapid cell performance deterioration at high temperatures (>60 °C),[9] compromising safety during operation and in the recycling process. In response to these challenges, the exploration of alternative fluorine-free salts in recent decades has led to the emergence of lithium bis(oxalato)borate (LiBOB) as one of the most promising and well-studied candidates.[10–15] Despite its lower solubility (0.8 M) and conductivity (8 – 9 mS cm^{-1}) in carbonate-based solvents compared to $LiPF_6$ (>1 M and >10 mS cm^{-1}),[16] LiBOB presents compelling features to address these limitations. It exhibits higher thermal stability, up to 300 °C, and decomposition products with lower toxicity than the fluorinated counterparts (B_2O_3 and CO_2).[10,17] Furthermore, LiBOB has gained environmental recognition, being classified as readily biodegradable in water by the European Chemicals Agency.[16] This classification ensures rapid and complete biodegradation

Z. Lu, S. Tardif
Univ. Grenoble Alpes, CEA, IRIG, MEM
Grenoble 38054, France
E-mail: samuel.tardif@cea.fr
T. Patranika, A. J. Naylor, J. Mindemark, G. Hernández
Department of Chemistry – Ångström Laboratory
Uppsala University
Uppsala SE-751 21, Sweden
E-mail: guiomar.hernandez@kemi.uu.se
S. Lyonnard
Univ. Grenoble Alpes, CEA, CNRS, IRIG, SyMMES
Grenoble 38054, France
E-mail: sandrine.lyonnard@cea.fr

The ORCID identification number(s) for the author(s) of this article can be found under https://doi.org/10.1002/smll.202410654

DOI: 10.1002/smll.202410654

in aerobic aquatic environments, aligning with the Organisation for Economic Cooperation and Development guidelines.[18] Moreover, the utilization of LiBOB has been widely reported to enhance battery performance by forming a stable solid electrolyte interphase (SEI) on the graphite electrode[10,12,15,19,20] and being able to further suppress electrolyte reduction and associated gas evolution.[21] This SEI predominantly consists of oxalates, semicarbonates, and ethers with polymer-like species,[11,13,22,23] further emphasizing the multifaceted advantages of LiBOB in enhancing both the safety and performance aspects of LIBs.

In the development of higher-performance LIBs with greater energy density, substantial efforts have additionally been devoted to the implementation of active materials with higher specific capacity and cycle life. Silicon stands out as one of the most promising candidates for the next generation of anode materials due to its exceptionally high theoretical capacity (3579 mAh g^{-1}), tenfold larger than the state-of-the-art graphite anode (372 mAh g^{-1}). However, the transformative potential of Si electrodes is hindered by its substantial volume expansion of up to 300% during lithiation.[24–26] This drastic expansion induces mechanical stress, leading to the pulverization of Si particles, loss of electrical contact, and the continuous growth of the SEI.[27] This drawback can be mitigated by introducing electrolyte additives, such as fluoroethylene carbonate (FEC)[28–31] and vinylene carbonate (VC)[32] to form a robust SEI layer. Furthermore, Si-based anodes have shown promising cyclability and electrochemical performance in LiBOB-based electrolytes. Investigations on the surfaces of Si thin films cycled in LiBOB-based and $LiPF_6$-based electrolytes using FTIR and XPS by Choi et al. revealed that the LiBOB-based electrolyte resulted in a less porous structure, contrasting with the moss-like, porous structure observed in $LiPF_6$ due to Si cracking.[33] Li et al. explored the electrochemical performance of Si/Graphite composite electrodes cycled in LiBOB and $LiPF_6$ mixed electrolytes, highlighting the role of LiBOB in forming an intact SEI layer and enhancing electrochemical performance.[34] However, other studies have shown the preferential degradation of LiBOB on graphite particles compared to silicon particles, which suggests that the formation of an SEI on graphite could leave the silicon particles unprotected.[23] Moving toward high-energy-density full cells (NMC111/Si-Graphite), Hernández et al. demonstrated that using a LiBOB-based electrolyte provided favorable electrochemical performance.[16] The LiBOB-based electrolyte showed higher cycling stability compared to a $LiPF_6$-based electrolyte without additives and at lower C-rates (C/10). However, at higher C-rates (C/2) the fluorine-free electrolyte featured lower performance due to its higher cell resistance. Collectively, these studies underscore the pivotal role of LiBOB in forming a robust and stable SEI on graphite, contributing significantly to improving battery performance. However, a thorough investigation dedicated to understanding the formation and growth of the SEI on silicon electrodes in LiBOB-based electrolytes and the role of additives remains noticeably absent in the current literature.

Indeed, the study of the SEI is crucial for advancing battery technology. However, obtaining reliable experimental data poses significant challenges. Traditional ex situ techniques often struggle to capture the dynamic nature of SEI evolution during cycling, leading to uncertainties in the obtained data. Synchrotron X-ray techniques are invaluable for *operando* battery characterization due to their ability to provide a dynamic view of a battery and its components during cycling, revealing real-time electrochemical mechanisms and processes often out of equilibrium.[35] A wide range of synchrotron-based techniques, such as small-angle X-ray scattering,[36] X-ray absorption spectroscopy,[37] and X-ray diffraction,[38] have been employed for battery characterization under *operando* or ex situ conditions. Additionally, X-ray reflectivity (XRR) and X-ray photoelectron spectroscopy (XPS) are particularly well-suited for SEI characterization due to their surface-sensitive nature, making them ideal for analyzing the physical and chemical responses at battery surfaces and interfaces. By combining their strengths, the integration of *operando* synchrotron XRR with ex situ XPS emerges as a powerful strategy.[39] The high intensity of X-rays generated by a synchrotron radiation facility enables fast XRR acquisition, facilitating *operando* experiments in battery research. *Operando* XRR provides real-time insights into interfacial phenomena, providing thickness, roughness, and electron density evolution during cycling, while ex situ XPS offers detailed chemical analysis post-cycling, creating a comprehensive approach for SEI dynamics and composition. In 2016 and 2017, Cao et al. investigated the lithiation mechanism of crystalline Si wafers at the atomic scale by the synchrotron XRR technique.[40,41] Furthermore, in 2017 and 2019, Veith et al. and Cao et al. respectively reported the investigation of SEI on Si anodes in $LiPF_6$-based electrolytes by performing *operando* neutron reflectivity and synchrotron XRR coupled with ex situ XPS experiments.[42,43] The former study explored the influence of FEC on the thickness and composition of the SEI, revealing that FEC decomposition results in a thinner SEI composed of more flexible polymeric components. The latter study focused on SEI formation, identifying two distinct layers: a top-SEI primarily composed of lithium fluoride (LiF), and a bottom-SEI consisting of lithiated species from the native oxide layer of the Si anode. Both studies integrated structural insights from reflectometry techniques with chemical information from XPS, highlighting the emerging trend of combining these methodologies for comprehensive SEI investigations.

Herein, we employ a combination of *operando* XRR and ex situ XPS to thoroughly investigate the formation and growth of the SEI on Si wafers with fluorine-free LiBOB-based electrolytes with and without vinylene carbonate (VC) as additive (illustration of the setup is shown in **Figure 1**). Hard X-ray Photoelectron Spectroscopy (HAXPES) at 7.05 keV, 2.35 keV, and Soft X-ray Photoelectron Spectroscopy (SOXPES) were used for probing different depths. The results are compared to investigate the impact and degradation of the salt, as well as the impact of the additive on the SEI formation and its dynamics. We find that both the composition and morphology of the SEI formed with LiBOB-based electrolytes differ from the SEI formed using $LiPF_6$-based electrolytes, and that the additive plays a subtle role that can lead to a more stable interphase and improved electrochemical performance.

2. Results and Discussion

To measure both the chemical and structural characteristics of the SEI formed on a silicon wafer using a fluorine-free electrolyte, two correlatively synchrotron experiments were performed, as

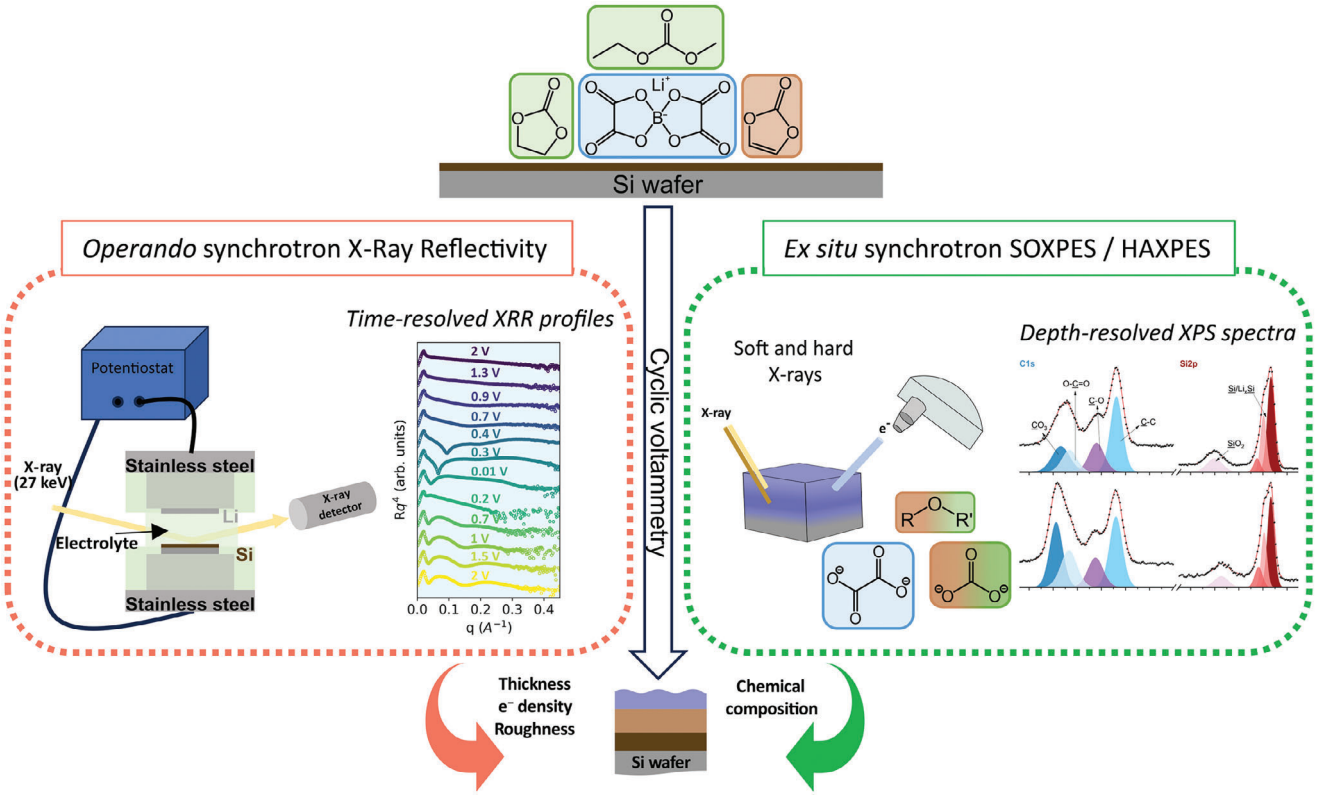

Figure 1. Schematic illustration of the measurement setup for XRR and HAXPS/SOXPES. A correlative analysis of the datasets and results is performed to determine the main structural and chemical characteristics of the SEI formed on silicon wafers using non-fluorinated electrolytes.

shown in Figure 1. XRR profiles and depth-resolved XPS spectra provide key parameters that are integrated to fully establish what are the properties of the SEI and how they are influenced by the use of an additive.

2.1. Electrochemical Responses

The *operando* cell for XRR has a large physical distance between the lithium foil and the working electrode, that is, the silicon wafer, to allow beam entry and reflection. While this setup is essential for obtaining XRR measurements, it compromises electrochemical performance by introducing higher resistance and reducing cell tightness compared to the pouch cells used for XPS. Additionally, since this setup is not optimized for electrochemical performance, maintaining consistent tightness of *operando* cells across different cells is challenging. Consequently, the LiBOB cell exhibits a significant negative parasitic current during both cathodic and anodic sweeps, which is less pronounced in the LiBOB+VC cell.

The electrochemical performance of both electrolytes was compared using cyclic voltammetry (CV), to control the time during the *operando* synchrotron XRR experiments. The cell setup for *operando* XRR (CV-XRR) is different from the cells for ex situ XPS (CV-XPS), and therefore slight differences are observed in the electrochemical response. **Figure 2** shows the cyclic voltammetry for CV-XPS and Figure S2 (Supporting Information) shows it together with CV-XRR. All potentials are given versus Li^+/Li unless otherwise stated. The overall intensity of the voltammogram is similar to the initial cycles for the two electrolytes. However, upon continuous cycling, the differences increase and the current is lower for LiBOB+VC compared to LiBOB (cycle 10 in Figure 2). This is an indication that LiBOB+VC does not lithiate the wafer to the same extent as LiBOB alone. Hence, the presence of VC changes the electrochemical response in the long term. Despite the differences between CV-XRR and CV-XPS (Figure S2, Supporting Information) due to the cell setup, performance is comparable and the focus of this project is on the SEI formation and growth, and not lithiation of the silicon bulk.

Looking closer to the initial cycle (Figure 2 inset) both voltammograms show a broad peak starting approximately at 1.8 V, corresponding to the initial formation of the SEI. This decomposition only occurs in the first cycle, as it is not visible in subsequent cycles. The current response is slightly higher in the case of LiBOB+VC which could be due to an initial decomposition of VC additive followed by the decomposition of LiBOB taking place also in the electrolyte without VC.[21,44] At the lower potentials (0.05 V) a reduction peak is seen, attributed to the lithiation of the crystalline silicon. As known from literature,[45,46] alloying materials, such as silicon become amorphous upon cycling. Hence, the reduction peak in the third cycle, seen at ≈0.15–0.2 V is attributed to the lithiation of the amorphous silicon.[47,48] This peak appears slightly later for LiBOB, which could be due to slightly higher resistance with this electrolyte compared to LiBOB+VC. Throughout cycling, the 10th cycle shows mainly a reduction peak

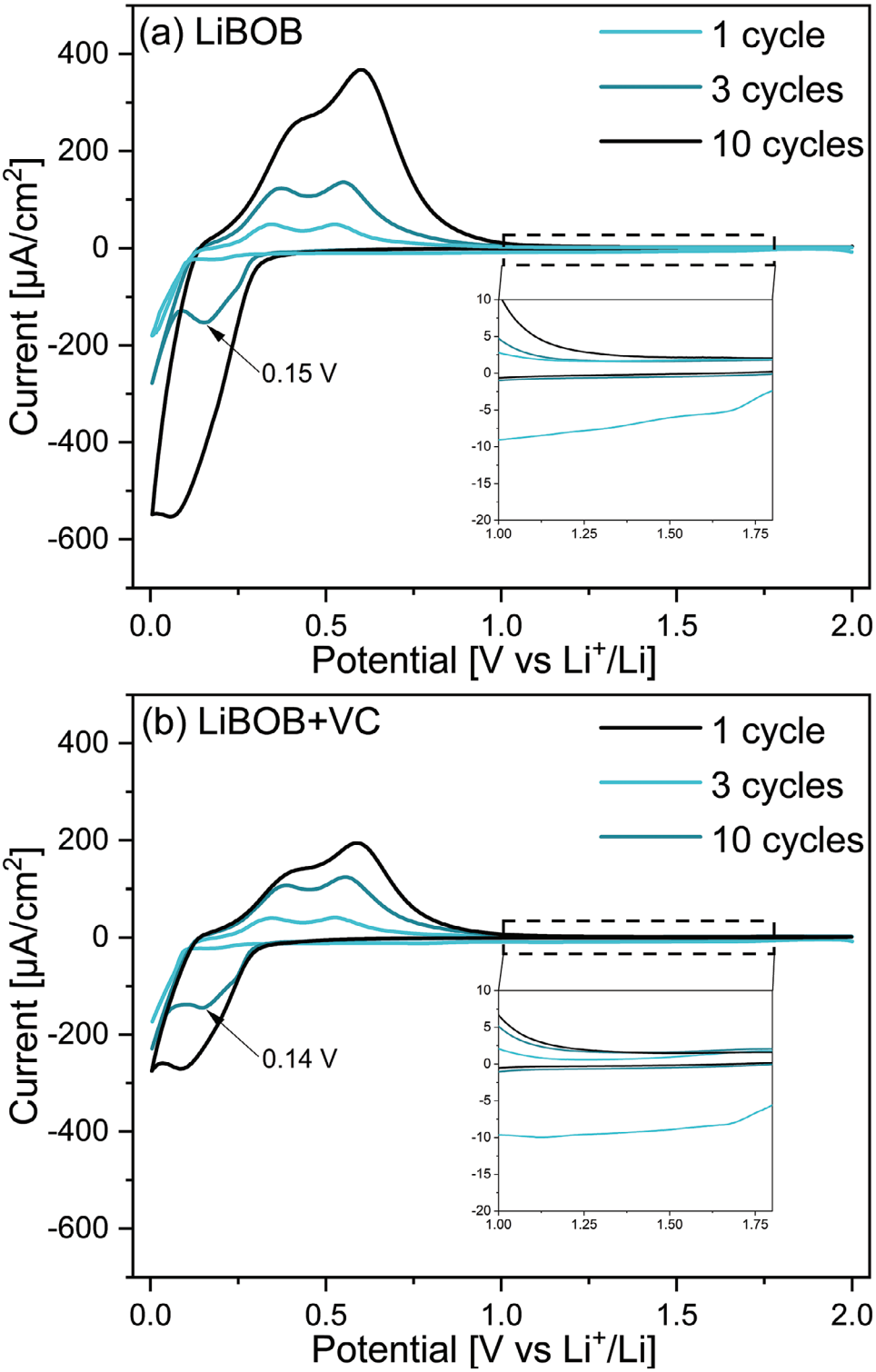

Figure 2. Cyclic voltammograms of the 1st, 3rd and 10th cycle of a) LiBOB and b) LiBOB+VC of the CV-XPS cell.

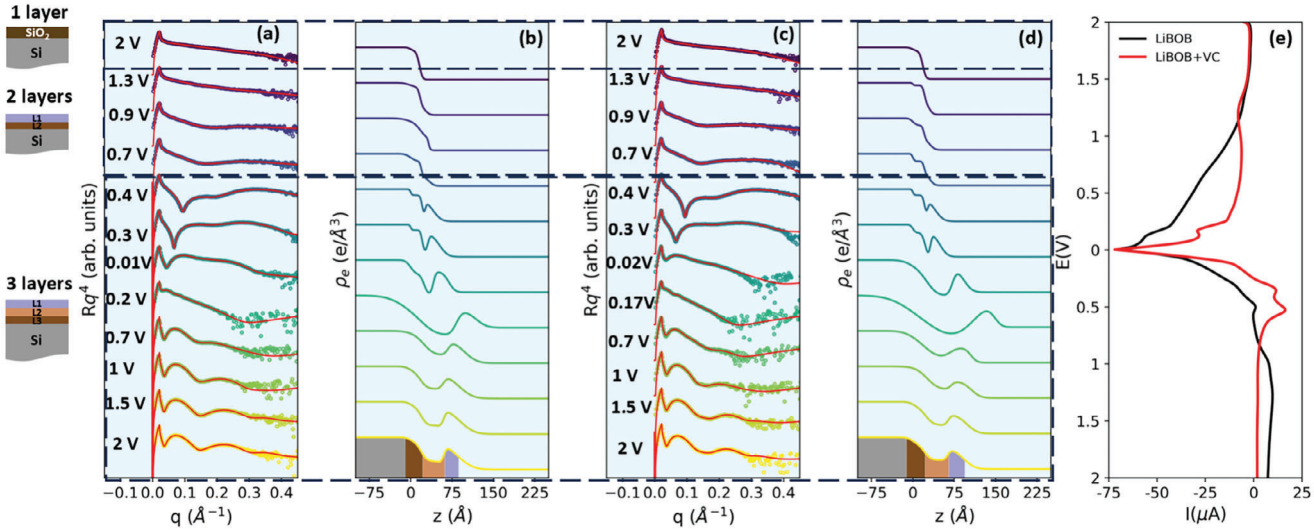

Figure 3. Experimental Fresnel-normalized XRR data (markers) and the corresponding fits (red solid lines) of a) LiBOB cell and (c) LiBOB+VC cell during the first cycle; (b) and (d) the corresponding fit-derived EDPs. All curves are vertically shifted for clarity. The left panel indicates the used XRR fitting models with 1, 2, or 3 layers on top of the silicon wafer. The layer L1 is assigned to the SEI while the layers L2 and L3 are assigned to lithiated SiO_2 and Si. e) Cyclic voltammograms of the first cycle of LiBOB cell (black line) and LiBOB+VC cell (red line).

of amorphous silicon being lithiated, showing less crystalline silicon remaining. The two oxidation peaks are also observed ≈ 0.3 and 0.5 V attributed to the delithiation of silicon.[48] These peaks show a slightly lower current for LiBOB compared to LiBOB+VC, indicating a lower delithiation degree or lithium being trapped.

Considering the CV-XRR cells in Figure S2 (Supporting Information), the electrochemical response shares some key features, aside from the parasitic current mentioned. A small negative current bump is observed ≈ 1.3 V during the cathodic sweep, which can be attributed to the formation of SEI, given that LiBOB decomposition begins ≈ 1.8 V, as seen in CV-XPS and reported in the literature.[14,21] Additionally, a reduction peak appears around 0.2 V in the cathodic sweep, and two oxidation peaks are observed around 0.3 and 0.5 V in the anodic sweep corresponding to the lithiation and delithiation of the silicon wafer as seen in CV-XPS. Even though the LiBOB cell exhibits parasitic current, the XRR datasets from both the LiBOB and LiBOB+VC cells show a high degree of similarity. This suggests that the parasitic current does not significantly influence the formation or evolution of the SEI at the electrolyte/electrode interface, but rather affects the lithiation of the bulk silicon, which is not the primary focus of this study. Therefore, our analysis will concentrate on the formation and evolution of the SEI and the (de)lithiation of the silicon surface and not the bulk.

2.2. Structural Characterization with *Operando* XRR

2.2.1. Qualitative Analysis

Figure 3a,c shows the measured Fresnel normalized XRR data (markers) at different selected potentials and their best fits (red lines) of the LiBOB cell and LiBOB+VC cell, respectively, during the first cycle. The fits-derived electron density profiles (EDPs) are present in Figure 3b,d. The cyclic voltammograms of the first cycle of LiBOB and LiBOB+VC cells are shown in Figure 3e. The full dataset is shown in Figures S3 and S4 (Supporting Information).

To gain further insights into the working electrode surface evolution, different XRR fitting models have been used throughout the cycling as shown in the left panel in Figure 3. From 2 to 1.4 V, the XRR data is fitted by a one-layer model sandwiched between the substrate (Si wafer) and the ambient (electrolyte). Here, this single layer corresponds to the native SiO_2 layer at the surface of the Si wafer. Note that it is reported in the literature that a thin layer should be added between the native SiO_2 layer and the Si wafer to have a precise simulation of the Si/SiO_2 interface for high q range XRR measurement (q_{max} up to 0.8 $Å^{-1}$).[49] Since the q range in this study is only up to 0.4 $Å^{-1}$, a single-layer model is sufficient to fit the Si/SiO_2 interface.

From 1.3 to 0.7 V, a minimum of intensity appears around $q_{min} = 0.15$ $Å^{-1}$, which corresponds to a thickness of $\frac{\pi}{q_{min}} \approx 21$ Å. These curves are well described by a two-layer model. The topmost layer represents the initially formed SEI at the interface between the surface of the SiO_2-terminated Si wafer and the electrolyte. The underlying layer, designated as L2, corresponds to the lithiated SiO_2 layer (Li_xSiO_y) on the Si substrate. This interpretation is consistent with the electrochemical response observed in the cyclic voltammograms (Figure 3e), where a small negative current bump is evident, indicating the formation of the SEI.

From 0.7 to 0.4 V, the previous q_{min} shifts to $q = 0.1$ $Å^{-1}$ accompanied by the appearance of another minimum around $q =$ 0.2 $Å^{-1}$. This indicates the appearance of another layer within the electrode, attributed to the further lithiation of SiO_2 and Si wafer.[41,42,50] It is important to note that in XRR fittings, the electron density profile is constructed by several layers, each with uniform electron density. To better describe this evolution of electrode surface, a more complex three-layer model is necessary to fit the XRR data from this stage. Assigning chemical components

to each layer based solely on their electron densities is challenging, even with prior information from the literature. The topmost layer remains representative of the SEI. Beneath the SEI, two additional layers designated as L2 and L3 are attributed to describing the increased variation of electron density above the intact bulk Si, corresponding to species with different degrees of lithiation. The L2 layer can be assigned to a portion of the more highly lithiated Li_xSiO_y, while the L3 layer can be assigned to the other side products of SiO_2 that are less lithiated and/or the diffusion of lithium into the bulk Si as proposed by Toney et al.[40–42] This three-layer model is extended to fit the XRR data for the remainder of the cycling process, covering the cathodic sweep from 0.4 V to complete anodic sweep as indicated in the left panel of Figure 3.

From 0.4 V to the end of the first cathodic sweep (≈0.01 V), the q_{min} shifts toward the lower q region, which suggests an increase in the thickness of the layers as the lithiation progresses further. This evolution in thickness correlates with the reduction peak around 0.05 V observed in the cathodic sweep of the cyclic voltammograms, signifying the lithiation of Si. The trend of increasing thickness persists until reaching 0.2 V during the subsequent anodic sweep. The observed hysteresis phenomenon can be attributed to the fact that, at the onset of the anodic sweep, the current to the working electrode remains negative. During the subsequent anodic sweep from 0.2 to 2 V, the q_{min} shifts back toward the higher q region, indicating the shrinkage of layers. This shrinkage correlates with the two oxidation peaks observed in the cyclic voltammograms around 0.5 V, which correspond to the delithiation of Si. The shrinkage continues until ≈1 V, where a second minimum emerges around $q = 0.15$ Å^{-1}, resulting in two fringes with different widths. This suggests that the probed surface presents two distinct electron contrasts. Indeed, the best fit-derived EDPs (see Figure 3b,d) show that the L2 layer presents a low-density layer, e.g. a distinct electron contrast with the adjacent layers.

2.2.2. Quantitative Analysis

Detailed quantitative results obtained from the XRR fittings of LiBOB and LiBOB+VC cells are presented in **Figure 4**. These results offer structural information on the electrode/electrolyte interface all along the first cycle, e.g. evaluation of layers thickness, averaged electron density, and roughness. Overall, the quantitative results of LiBOB and LiBOB+VC cells show high similarity and only subtle differences are observed.

LiBOB Cell: We first focus on the XRR fitting results of the LiBOB cell. The topmost layer, at the interface between the wafer and the electrolyte, is assigned to the SEI. Its thickness, electron density, and roughness during the first cycle are shown in Figure 4a. Its evolution during the first cycle can be divided into three stages: I. formation and initial growth; II. densification and continuous growth; III. partial dissolution or shrinkage. During stage I, that is, from 1.3 to 0.5 V, the thickness of the SEI increases from 9 to 15 Å, with an electron density ≈ 0.48 e Å^{-3}. Its roughness varies ≈ 7 Å. At this stage, the evolution of SEI density and roughness shows dynamic fluctuations, indicating a variable nature of the initial SEI formation process. From 0.6 to 0.5 V, a significant increase in SEI electron density is observed from 0.48 to 0.6 e Å^{-3}. This indicates that the SEI has progressed to stage II. During stage II, from 0.5 V to the end of the cathodic sweep, the SEI thickness increases to 28 Å while its electron density stays ≈ 0.6 e Å^{-3}. At the beginning of the anodic sweep (0.1 V), as expected from XRR raw data, a remarkable increase of SEI thickness from 28 Å to 36 Å is observed accompanied by a slight decrease in electron density to 0.57 e Å^{-3}. As the delithiation process continues, the SEI transitions into stage III, characterized by a gradual and consistent decrease in thickness from 36 to 25 Å. Simultaneously, there is an increase in both density and roughness, with density rising from 0.57 to 0.65 e Å^{-3} and roughness expanding from 17 to 21 Å. By combining the lithiation results, we observe a distinct "breathing behavior" in the thickness of the SEI layer. This effect is further supported by the evolution of the density-thickness product shown in Figure S5 (Supporting Information), a reliable parameter derived from XRR fits that allows us to evaluate the total number of electrons per unit surface in the SEI layer. Notably, the density-thickness product increases during the cathodic sweep and decreases during the anodic sweep, likely attributed to the incorporation and dissolution of decomposition products of electrolytes into the SEI. This assumption is further investigated by XPS analysis and will be presented in the following section.

Then we turn to the L2 layer, just below the SEI. From OCV to 1.3 V, the L2 layer remains consistent with a density of 0.66 e/Å^3, a thickness of ≈16 Å, and a roughness of ≈5 Å. These findings suggest that the L2 layer corresponds to the native SiO_2 layer in this voltage range, indicating that lithiation of SiO_2 has not yet taken place. Afterward, from 1.3 to 0.55 V, which is within stage I of the SEI, the L2 layer thickness increases slightly from 16 to 19 Å, with a slight decrease in density to 0.62 e Å^{-3}. This stage may be assigned to the initial lithiation of the SiO_2 layer (Li_xSiO_y), as expected.[51] Further lithiation of SiO_2 and the underlying Si layer is observed from 0.55 V, extending until ≈0.1 V of the anodic sweep. At 0.55 V, an additional layer L3 is needed to fit the experimental data. As explained in the "Qualitative analysis" section, the lithiation process leads to the increase of chemical inhomogeneity of the SiO_2/Si interface, resulting in the formation of lithiated SiO_2 along with side products Si and lithiated Si.[42] Additionally, the diffusion of lithium in bulk Si increases the electron density complexity at this interface. These factors necessitate the inclusion of another layer in the fitting model. Therefore, starting from 0.55 V, L2 and L3 are used to describe the lithiated SiO_2/Si layers between the SEI and the intact bulk Si. Note that the nature of L2 and L3 are interconnected, as these layers represent electron density gradients introduced along the formation of lithiated phases in both SiO_2 and Si. Accordingly, variations in local single-layer thickness, for instance, do not describe a single process, but rather account for the evolution of the amount of lithiated phases close to the SEI and/or close to the silicon wafer. Therefore, from 0.55 V, L2 is assigned to a layer containing chemical components with lower electron density. The original thickness of this low-density layer is 2 Å with an electron density of 0.47 e Å^{-3} compared to L3 (0.67 e Å^{-3}). Consequently, at this potential, L2 is associated with a layer containing Li_xSiO_2 species with lower electron density and a high degree of lithiation, while L3 can be assigned to a layer containing Li_xSiO_y species with lower lithiation degree and/or lithiated Si.

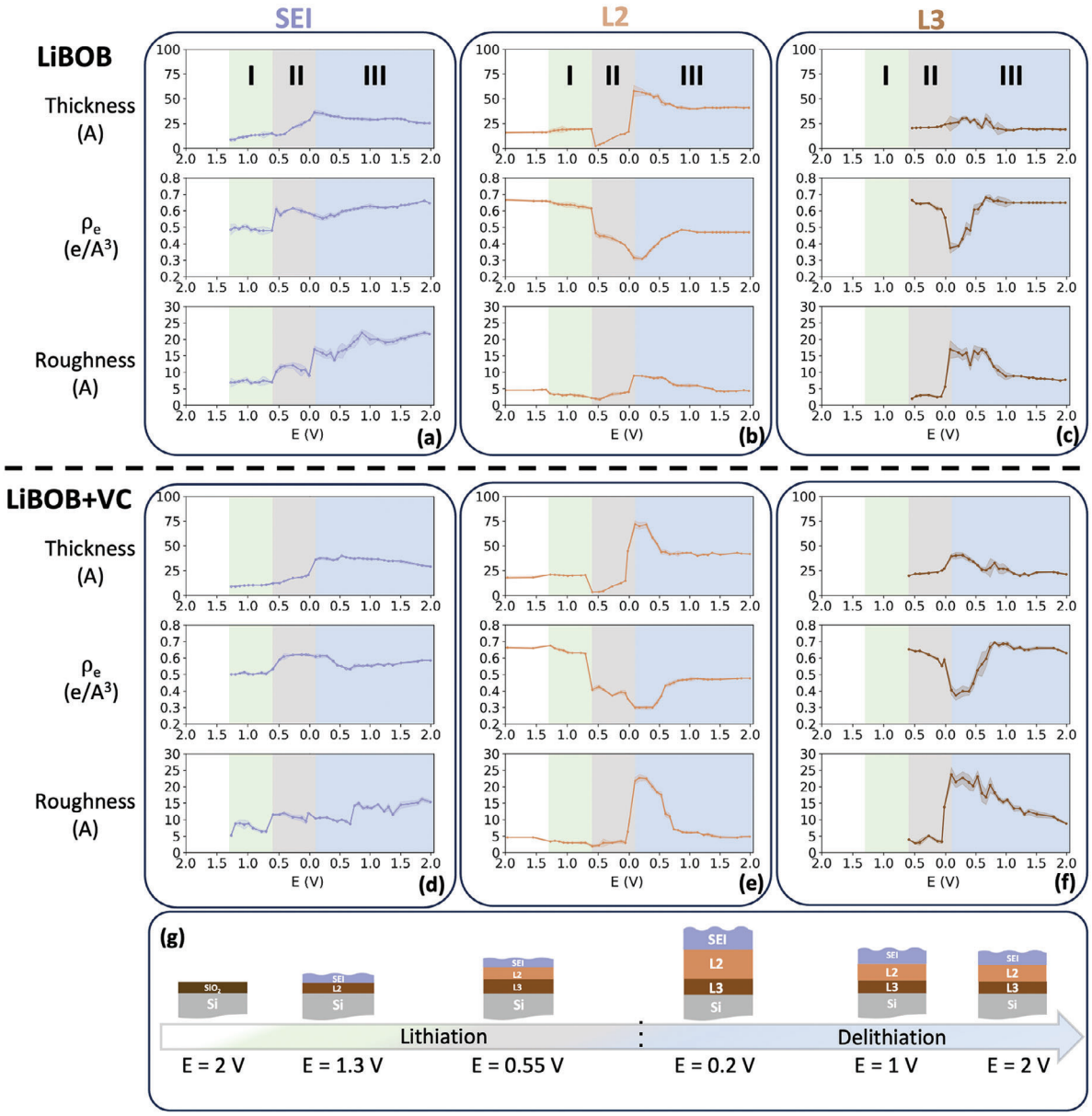

Figure 4. Quantitative results from first-cycle XRR fits: a–c) Thickness, electron density, and roughness of SEI, L2, and L3 layers, respectively for the LiBOB cell; d–f) Same parameters for the LiBOB+VC cell; g) schematic view of Si surface evolution in the LiBOB cell. The numbered regions (I, II, III) with different background colors indicate the different stages of electrolyte/electrode interface evolution. The first layer is the SEI layer while L2 and L3 correspond to different lithiated silicon phases between the SEI and the bulk wafer.

The chemical compositions of these two layers evolve during cycling as indicated by the different electron densities. In the later lithiation process, the L2 layer undergoes continuous expansion, reaching a thickness of 58 Å, while its density decreases from 0.47 to 0.31 e Å^{-3}. Comparing these values with the nominal density of Li_xSiO_y (ca. 0.7 e Å^{-3}) and that of Li_xSi (<0.4 e Å^{-3}),[42] it can be inferred that the predominant component within the L2 layer at the end of stage II evolves from Li_xSiO_y to Li_xSi and Li_2O. During the subsequent anodic sweep, the thickness of the L2 layer continues to decrease steadily to 41 Å, accompanied by an increase in density to 0.47 e Å^{-3}. Thus, a "breathing behavior" of the electrode is observed during the first cycle, with some compounds being dissolved back into the electrolyte. Furthermore, it is intriguing to note that the density of the L2 layer at the end of the anodic sweep is notably lower than the density of Si (0.7 e Å^{-3}) or amorphous Si after cycling (0.64–0.67 e Å^{-3}).[41] This lower-density characteristic can potentially be explained by the trapping of lithium in the electrode.[52]

Finally, we turn to the late-appearing layer L3, located just above the Si substrate. As mentioned previously, the incorporation of L3 into the XRR fitting model from 0.55 V during the cathodic sweep aims to provide a more accurate description of the complex electron density within the lithiated SiO_2/Si layers. The evolution of the L3 layer during the first cycle does not exhibit

distinct stages like the SEI or L2 layers. Its thickness varies between 20 and 30 Å throughout, while its density decreases from 0.68 to 0.38 e $Å^{-3}$ during the cathodic sweep and then increases to 0.65 e $Å^{-3}$ during the anodic sweep. This evolution can be attributed to the (de)lithiation of the bulk Si substrate. Consequently, the L3 layer can be considered as the lithiated part of the Si bulk, situated between the intact bulk Si substrate and the lithiated SiO_2 layer/Si surface (L2). Unlike in L2, the electron density of L3 (≈0.65 e $Å^{-3}$) at the end of the first cycle is higher than that of L2 (≈0.47 e $Å^{-3}$). Given that the electron density of L3 at this point closely matches the electron density of amorphous Si reported by Cao et al.,[41] we attribute L3 to amorphous Si at the end of the first cycle.

LiBOB+VC Cell: The quantitative XRR fitting results of the LiBOB+VC cell show similarities to those of the LiBOB cell, revealing a three-stage evolution in the SEI and "breathing behavior" in both the SEI and L2 layers during cycling (Figure 4). Notably, the SEI layer in the LiBOB+VC cell ends up at the first cycle with a slightly increased thickness of 29 Å compared to the LiBOB cell (25 Å), while its density is lower (0.59 e $Å^{-3}$) compared to the LiBOB cell (0.65 e $Å^{-3}$). Additionally, the roughness of the SEI layer in the LiBOB+VC cell during the first cycle is consistently lower than in the LiBOB cell.

Concerning the L2 layer, there is a noticeable increase in thickness expansion at the end of stage II for LiBOB+VC (72 Å) compared to LiBOB (57 Å). A similar trend is observed for the L3 layer, with L3 expanding to a maximum of 40 Å in LiBOB+VC, while it remains ≈ 25 Å for LiBOB. These findings suggest that more electrode lithiation occurs in the LiBOB+VC cell compared to the LiBOB cell.

Upon comparing the results between LiBOB and LiBOB+VC, the XRR findings indicate that the addition of 2 wt% VC has a very subtle influence on the formation trend of the SEI layer in terms of structural characteristics (e.g., thickness, density, roughness). However, it plays a pivotal role in fostering the development of a smoother SEI layer and facilitating additional lithiation of the Si electrode within the LiBOB+VC cell. These subtle yet crucial structural variations observed between LiBOB and LiBOB+VC suggest the importance of VC as an additive. However, the XRR technique falls short in providing further insights into the origin of these subtle differences, as it solely probes the electron density of the sample surface using a layer-by-layer model without offering any chemical information. To delve deeper into its impact on the chemical compositions of the SEI and lithiated SiO_2/Si (L2 and L3 layers), further investigation through ex situ XPS is imperative and will be shown in the following section.

2.3. Surface Chemistry Characterization with Ex-Situ XPS

The XPS experiments were conducted using three energy regimes in order to probe several depths of the samples aiming to investigate the different layers observed with XRR. For the most surface-sensitive measurements, a constant kinetic energy of 200 eV was used, varying the photon energy for each core level, resulting in a consistent probing depth. The corresponding photon energy is shown in the respective spectrum. For the greater probing depths, 2.35 and 7.05 keV were used, with the probing depths corresponding to approximately L2 and L3, respectively, from the XRR results. For all samples, C 1s, O 1s, Si 2p, B 1s, and Li 1s core-levels were measured and the corresponding spectra are shown in full in Figures S6–S23 (Supporting Information). The three first-mentioned mentioned core-levels showed the most relevant information and will be discussed more in detail (Figures S6–S11, Supporting Information), whereas the B 1s and Li 1s did not show any significant difference (Figure S12–S23, Supporting Information). The potentials chosen for the XPS measurements were based on the results observed for XRR, where considerable differences were observed. Thereby, the chemical composition of the layers detected by XRR could be further investigated. The results are divided and discussed by the three stages in potentials previously described.

2.3.1. Stage I (1 to 0.5 V, Lithiation)

According to XRR, the formation of the SEI started at 1.3 V; therefore, the first potential probed with XPS was at a lower potential (1 V). The spectra of all photon energies (Figures S6–S11, Supporting Information) for both electrolytes are fairly similar with a large contribution of carbonates, especially at higher photon energies (Figures S10 and S11, Supporting Information). These results corroborate the XRR findings, indicating that the onset of SEI formation occurs before reaching 1 V.

The lithiation from 1 to 0.5 V (stage I) with the 2.35 keV energy for C 1s is shown in **Figure 5** and the complete C 1s spectra of all photon energies are shown in Figures S6–S11 (Supporting Information). In stage I, LiBOB shows more ester (O═C─O) build-up at the binding energy of 288.5 eV[53,54] compared to LiBOB+VC. In contrast, LiBOB+VC shows a buildup of carbonates (-CO_3) at 289.6 eV binding energy. One possible decomposition route of the BOB anion is a ring-opening reaction forming oxalates (shown as esters, O═C─O),[14,22,23] and carbonates (from CO_2 reduction products).[14,21,22] For the LiBOB+VC electrolyte, it is the VC reacting to form carbonate species, such as poly(VC)[55] or through ring-opening reactions.[56] Although ester groups are also seen with the LiBOB+VC electrolyte, the presence of VC seems to prevent the initial degradation of LiBOB to some extent.

Considering the Si 2p spectra of both electrolytes at 2.35 and 7.05 keV photon energies (Figures S8–S11, Supporting Information), the peak of the elemental silicon has a shoulder peak growing during stage I. This is suggested to be a result of elemental silicon being lithiated to different degrees since the lithiation within the wafer or silicon oxide layer is not necessarily evenly distributed. A general broadening of the silicon peaks is observed throughout the lithiation starting from 1 V, as suggested by XRR fittings and corresponding to L2 and L3. Additionally, a shift in the binding energies of the peaks is seen both for the elemental silicon and for the silicon oxide (101.8 eV), which has been reported as the silicon being lithiated.[51]

The O 1s spectra at 7.05 keV photon energy (Figures S10 and S11, Supporting Information) show Li_2O at the bulk of the wafer at a binding energy of 530 eV. The origin of Li_2O has been reported to form from the reaction of SiO_2 with lithium.[42,51,57–59] This Li_2O peak appears at higher potentials with LiBOB electrolyte (1 V) than with LiBOB+VC (0.5 V). This aligns with the observations from the Si 2p that the electrode materials in the

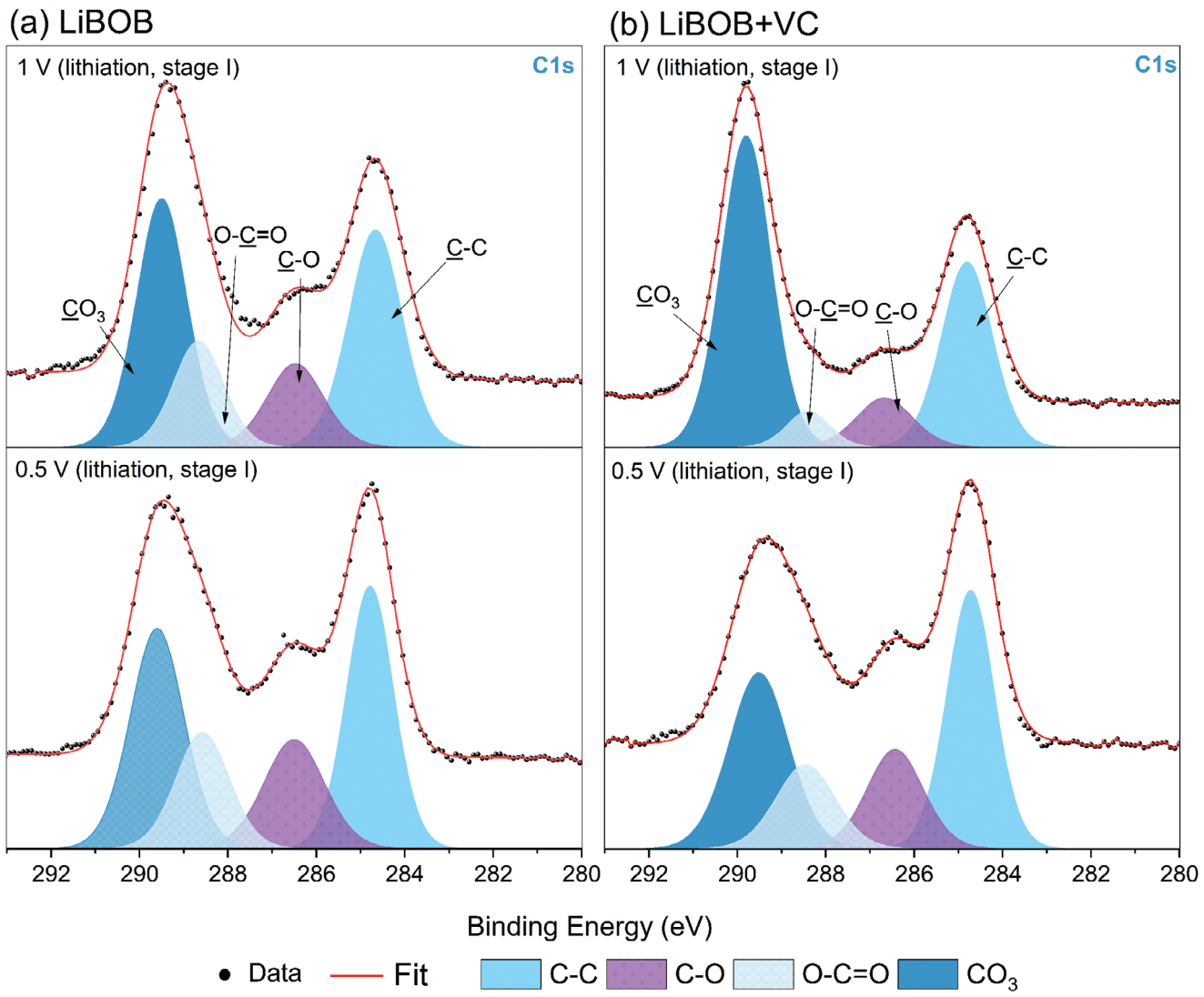

Figure 5. C 1s spectra of 2.35 keV photon energy in two potentials in stage I, 1 and 0.5 V during lithiation for a) LiBOB and b) LiBOB+VC.

LiBOB cell lithiates earlier and to a larger degree than with LiBOB+VC.

2.3.2. Stage II (0.3 to 0.05 V, Lithiation)

During stage II (0.3 – 0.05 V), the C 1s spectra for all the photon energies (Figures S6–S11, Supporting Information) of the LiBOB cell show a decrease in the ester groups and an increased carbonate peak, which is correlated to the decomposition of EC. This suggests that LiBOB is not able to form a stable SEI that prevents further electrolyte decomposition.[23] Instead, with LiBOB+VC the carbonate peaks increase from 0.3 to 0.14 V and then decrease at 0.05 V whereas there is a continuous growth of the ester peaks throughout the lithiation, which indicates decomposition of the BOB anion. Thereby, the VC that decomposed in stage I is also not able to prevent the decomposition of LiBOB later on.

Lithiation of the silicon phase continues as seen from the shoulder and the shift in the Si 2p spectra. Furthermore, the Si 2p spectra have more noise with the LiBOB electrolyte indicating a thicker SEI layer compared to LiBOB+VC. In the case of the O 1s spectra, despite the earlier appearance of Li_2O at 7.05 keV with LiBOB electrolyte, after the lithiation the corresponding peak is larger for LiBOB+VC (Figure S11, Supporting Information) and can be seen as well at 2.35 keV (Figure S9, Supporting Information), in agreement with the literature.[51]

2.3.3. Stage II → Stage III (0.05 to 0.2 V of Delithiation)

The O 1s, C 1s, and Si 2p spectra of the transition between stage II and III for the soft X-ray and 7.05 keV photon energy are shown in **Figure 6**. Larger differences between the electrolytes are seen in the peak intensities between the lithiation (0.05 V) and delithiation (0.2 V). In the C 1s soft X-ray measurements, carbonate species are present with LiBOB electrolyte although they decrease upon delithiation (Figure 6a), whereas in the case of LiBOB+VC, a carbonate peak is seen at 0.05 V but it is not

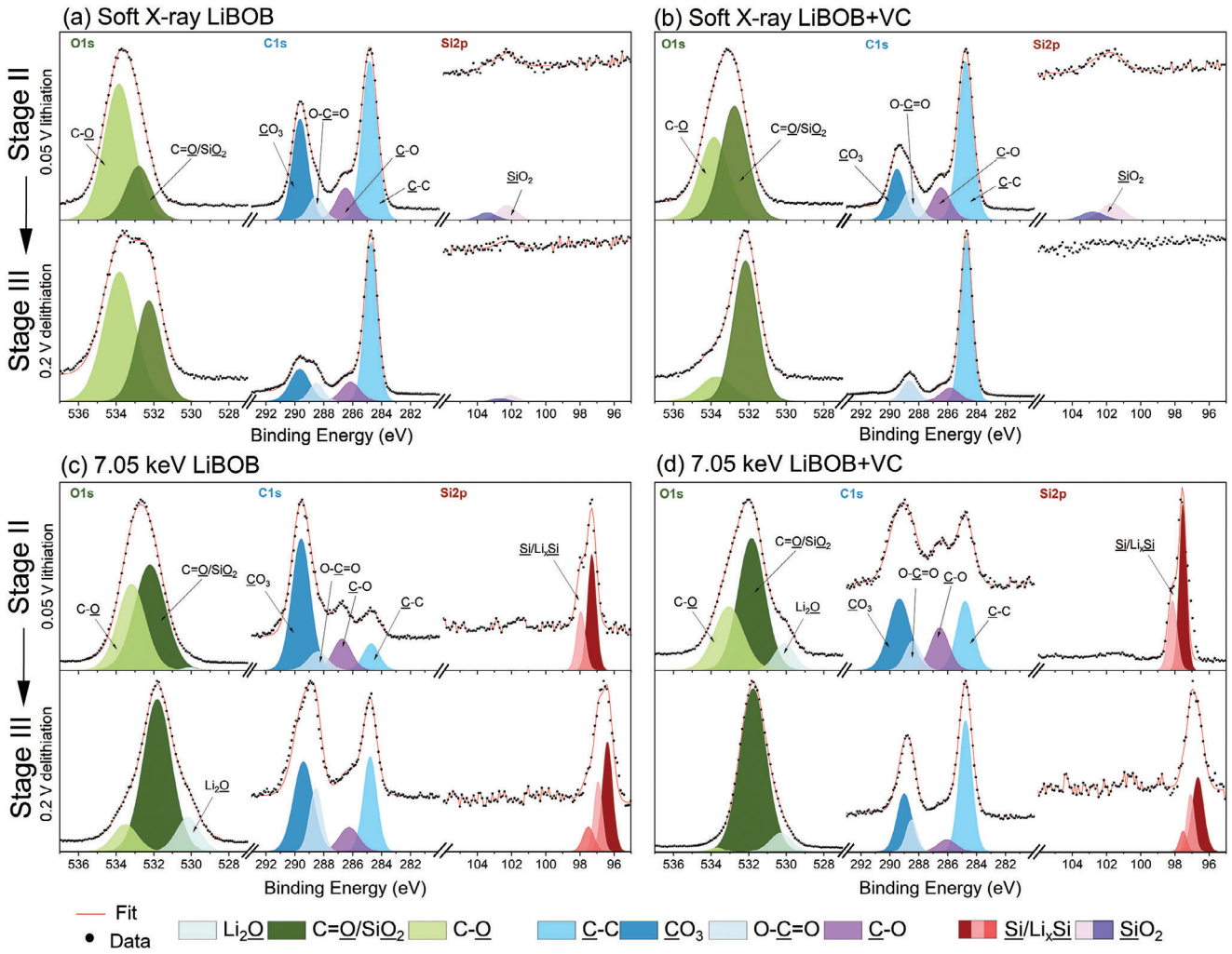

Figure 6. O 1s (0.75 keV), C 1s (0.505 keV) and Si 2p (0.3 keV) spectra of the soft X-ray for both electrolytes a) LiBOB and b) LiBOB+VC, and the 7.05 keV photon energy for the respective electrolytes (c) and (d) in the transition between stage II and III, that is, between the lithiation at 0.05 V and delithiation at 0.2 V.

visible at 0.2 V (Figure 6b). Moreover, soft X-ray photoelectrons of O 1s show slightly lower ether peaks (C—O)[60] at 533.6 eV for LiBOB+VC at 0.05 V compared to LiBOB (Figure 6a and b). For LiBOB+VC, the peak decreases significantly upon delithiation in stage III, in agreement with the carbonate peak disappearing in C 1s. This indicates that the carbonate species on the outer surface at 0.05 V are possibly dissolved back into the electrolyte, or reacting further. One possible decomposition product of lithium carbonate is lithium oxide,[61] and this peak increases at the same potential closer to the bulk in the O 1s spectrum (seen in Figure 6d). Furthermore, Figure 6a,b also show the Si 2p of the soft X-ray measurements. The peak of the silicon oxide and the noise ratio provide information about the thickness of the layers. The spectra have higher noise at the beginning of stage III (0.2 V during delithiation), indicating that the SEI is thickest at this potential, which correlates with the XRR data. For the soft X-ray photoelectron at 0.2 V during delithiation with LiBOB, a small peak of silicon oxide is visible at this potential, while for LiBOB+VC this is not the case. This further confirms LiBOB+VC having a thicker layer upon delithiation, as seen in the XRR data.

Figure 6c,d show the spectra at 7.05 keV photon energy, with a probing depth that reaches the lithiated silicon layers (L2 and L3), since the elemental silicon peaks are seen at 99 eV for both electrolytes in the Si 2p spectra. Looking at the C 1s spectra for the same photon energy, it can be seen that both electrolytes show carbonate peaks at the end of stage II and at the beginning of stage III, contrary to the observations in the surface spectra in Figure 6a,b. These carbonates could have been formed at the start of the lithiation, closest to the bulk, further confirmed by the carbonate being the main peak at 1 V during lithiation at all photon energies, seen in Figures S6–S11 (Supporting Information). Despite its disappearance from the outermost surface at the beginning of the delithiation in the LiBOB+VC electrolyte, these carbonate species remain present throughout the different samples and potentials. Moreover, it can be noted both for 2.35 and 7.05 keV that the ester peak at 288.5 eV for LiBOB+VC is pronounced at lithiation in stage II but decreases in magnitude upon

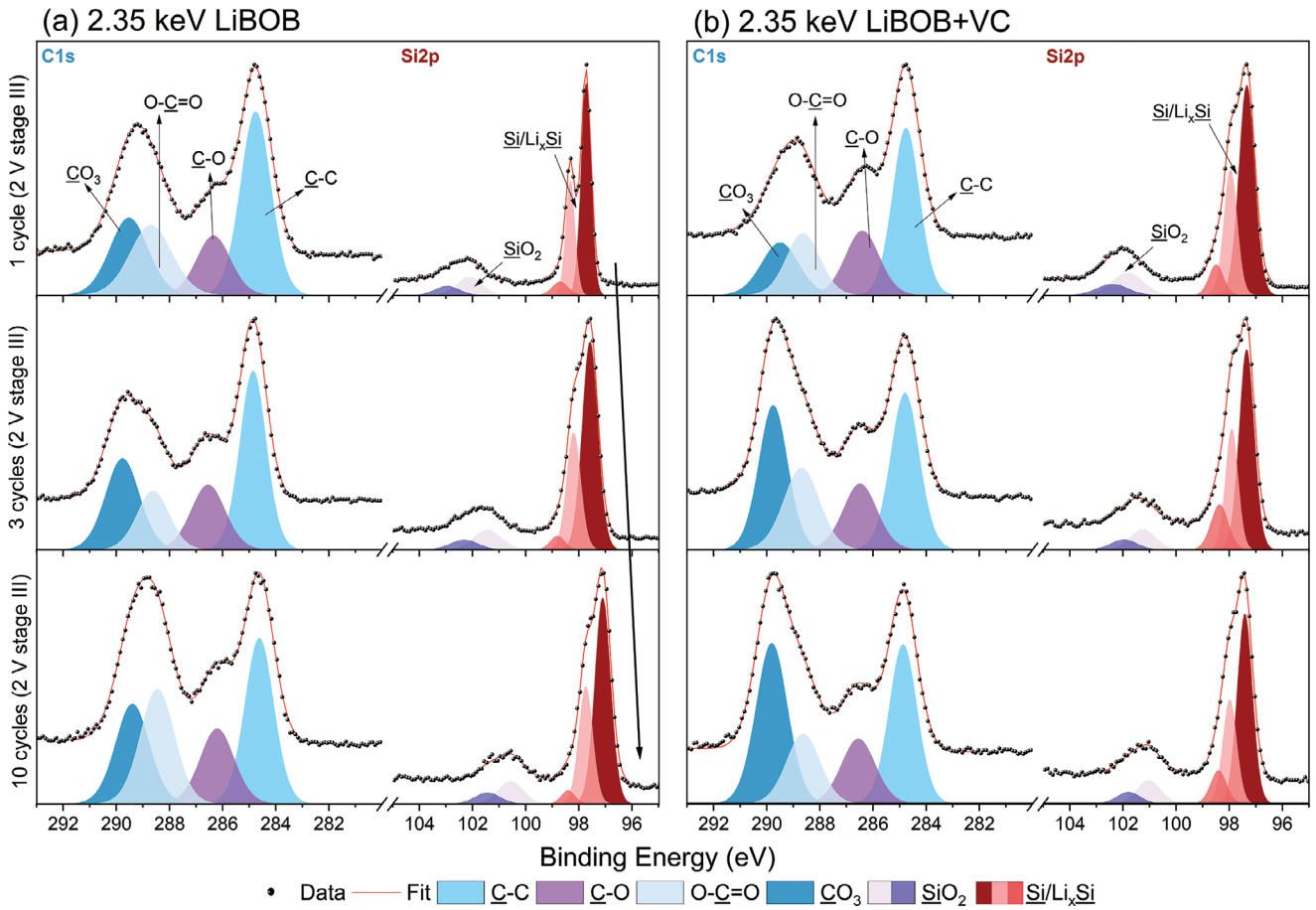

Figure 7. C 1s and Si 2p spectra at 2.35 keV photon energy for one, 3, and 10 full cycles, that is, end of stage III for a) LiBOB and b) LiBOB+VC. The arrow in the Si 2p spectra indicates the shift in binding energy upon cycling.

delithiation at 0.2 V and continuous to grow during the remaining delithiation in stage III. This is not the case for the LiBOB electrolyte, which shows lower amounts of esters at 0.05 V (lithiation) and thereafter an increased intensity at 0.2 V (delithiation). Hence, it could be interpreted that both electrolytes are decomposing the electrolyte salt, forming oxalates, but the additive in LiBOB+VC can limit the decomposition of LiBOB to some extent. The O 1s spectra at 7.05 keV photon energy (Figure 6c,d) show Li_2O at the bulk of the wafer, following what has been previously reported in the literature.[57,58,61] LiBOB+VC shows clear peaks of Li_2O both during the lithiation (0.05 V) and after (0.2 V). On the contrary, LiBOB shows a clearer peak of the Li_2O at the delithiation (0.2 V).

The shift toward lower binding energies observed in the Si 2p spectra for stages I and II continues until the first point of delithiation (0.2 V), where full lithiation of the SiO_2 layer is observed also from the disappearance of the peak seen with soft X-rays.

2.3.4. Stage III (0.2 to 2 V, Delithiation)

Stage III corresponds to the delithiation reaction. The C 1s spectra of the SEI for LiBOB show a decrease in the ester peaks and an increase in the carbonates, which is also observed at higher photon energies. Despite the decrease in carbonates at the beginning of the delithiation, these species form again on the surface. LiBOB+VC electrolyte features the opposite trend; ester peaks decrease while carbonates appear again at 1 V on the SEI during delithiation and the intensity increases throughout the delithiation and at higher photon energies.

Si 2p spectra show that silicon peaks shift back to higher binding energies although not to the original position, indicating that the wafers remain partly lithiated with both electrolytes. The peak corresponding to SiO_2 is seen again with 2.35 keV after disappearing at the end of the lithiation.

2.3.5. Cycles 1, 3, and 10 (2 V, Delithiation End of Stage III)

Figure 7 shows the C 1s and Si 2p spectra at 2.35 keV photon energy at the end of stage III for 1, 3, and 10 full cycles. After one full cycle, LiBOB shows a predominant carbonate peak at 289.5 eV while LiBOB+VC shows equal carbonates, esters (O—C═O), and ethers (C—O) in intensity. Furthermore, LiBOB shows a continued growth of the ester peak going from one to ten cycles (Figure 7a), while LiBOB+VC shows similar intensities of the ester and ether peaks but an increase in the carbonate peaks upon cycling (Figure 7b).

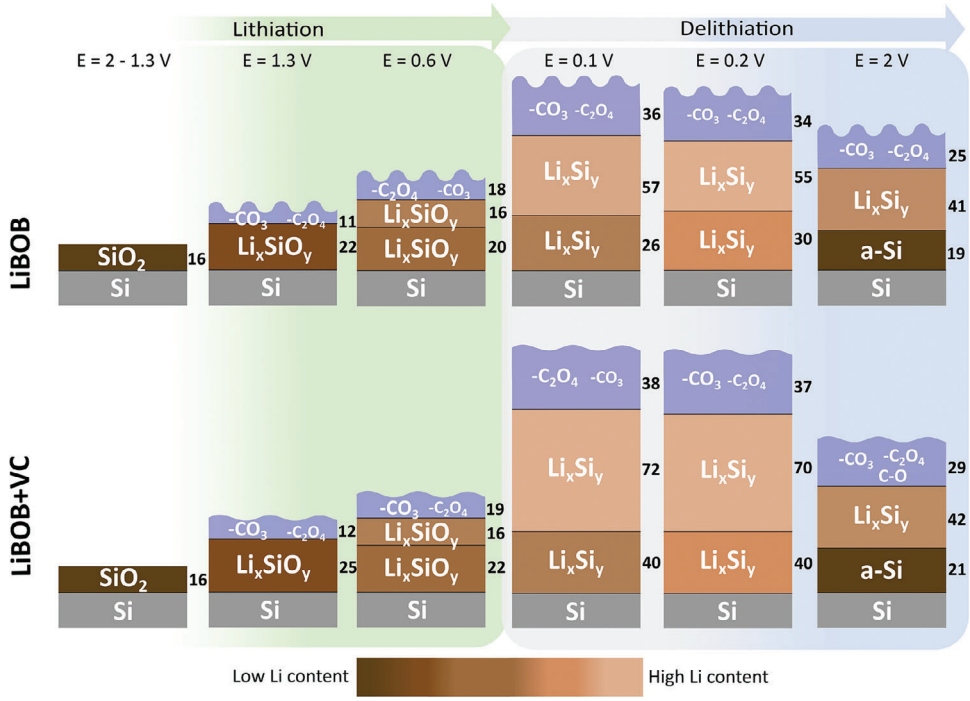

Figure 8. Schematic illustration of Si wafer surface evolution during cycling in LiBOB and LiBOB+VC. The font size in the SEI of each chemical component indicates their relative content. The thickness of each layer is given in Ångström (black values). The lithiation degree in the two lithiated silicon layers (L2 and L3) is indicated by the color gradient. At the end of the delithiation, L3 is an amorphous lithium-free silicon layer, while some lithium remains trapped in L2.

Looking at the Si 2p spectra in the case of the LiBOB electrolyte, comparing the spectra after 1, 3, and 10 cycles, there is still a shift toward lower binding energies at 2 V (Figure 7a). This indicates that the silicon is still partially lithiated at this stage, meaning that the wafer is not being fully delithiated at the end of each cycle and lithium is being trapped. This is not as pronounced in LiBOB+VC electrolyte (Figure 7b). Moreover, Li_2O is also observed to grow with the increasing cycle number with both electrolytes (Figures S8–S11, Supporting Information).

2.4. Correlation Between XRR and XPS Results

The structural information provided by *operando* XRR in combination with the chemical composition at different probing depths obtained from the ex situ XPS measurements contribute to understanding SEI formation and evolution of the LiBOB-based electrolyte, the surface evolution of the Si wafer during cycling, and the influence of the additive VC. A schematic representation of Si wafer surface evolution during its cycling in LiBOB-based electrolytes from XRR and XPS results is illustrated in **Figure 8**.

For both LiBOB-based electrolytes, the SEI evolution can be divided into three distinct stages. Stage I spans from 1.3 to 0.5 V, representing the initial formation of the SEI. XRR results indicate SEI formation onset at 1.3 V, coinciding with initial SiO_2 layer lithiation. This is corroborated by XPS spectra at 1 V, demonstrating oxalate and carbonate species in the SEI. Throughout stage I, XRR reveals a continuous increase in SEI thickness. XPS analysis shows more ester/oxalate species in the SEI formed with LiBOB, suggesting more BOB decomposition, while the LiBOB+VC electrolyte forms more carbonate species coming from VC decomposition, which are known to form a smooth polymeric layer.[16,23,62] This agrees with the XRR results that show slightly lower roughness in LiBOB+VC compared to LiBOB, whose roughness might come from the more inorganic oxalate/ester species. This highlights VC's role in inhibiting the initial LiBOB decomposition and promoting smoother SEI during early lithiation.

Concurrently, the lithiation of SiO_2/Si progresses, evident from the L2 layer electron density decrease and L3 layer emergence in the XRR fittings in stage II. Here, the slight decrease in electron density of L2 could be attributed to the amorphous nature of Li_xSiO_y.[42] As lithiation progresses, more products with lower density (Li_2O, Li_xSi) are incorporated into the L2 layer, leading to a decrease in electron density, as previously described. Even though we cannot distinguish the chemical compositions of lithiated layers quantitatively, by comparing the electron density of L2 and L3 layers with the reported data in the literature, we can deduce that Li_xSiO_y species are the main components in the L2 and L3 layers at this stage. This agrees with the XPS results, showing a consistent Si peak shift to lower binding energy already at 1 V (compared to the pristine wafer) and to 0.5 V, indicating SiO_2/Si lithiation. Furthermore, the Li_2O peak appears early during the lithiation step and aligns well with the reduction of silicon and lithium ($SiO_2 + 4Li \rightarrow Si + 2Li_2O$).[51] LiBOB cell starts lithiation at slightly higher potentials which explains the earlier appearance of Li_2O compared to the LiBOB+VC cell.

Stage II denotes the densification and further growth of the SEI, from 0.5 to 0.05 V of lithiation. The densification of the SEI

is observed for both electrolytes from 0.5 to 0.3 V, followed by consistent SEI thickness increase to its maximum at early delithiation (≈0.1 V). There is a change in SEI composition during stage II with carbonates dominating in the LiBOB cell and esters in the LiBOB+VC cell. This suggests that the solvents, EC and EMC, decompose forming carbonate species, and that the SEI layer formed from the decomposition of the BOB anion is not enough to prevent further electrolyte decomposition. Similar behavior is observed with LiBOB+VC; the initial SEI formed from VC is not able to protect the surface and further BOB decomposition is seen with this electrolyte as well. Concurrently, the thickness of lithiated SiO_2/Si layers (L2 and L3 layers) increases along the lithiation, reaching a maximum at 0.1 V of delithiation, with consistent electron density decrease. The low electron density (<0.4 e/Å^3) at the end of this stage suggests that the main chemical components of these two layers evolve from Li_xSiO_y to Li_xSi and Li_2O. The consistent shift of the Si 2p peak in XPS analysis from 0.5 V during lithiation to 0.2 V of delithiation corroborates the gradual lithiation of the Si wafer.

The transition from stage II (0.05 V lithiation) to stage III (0.2 V delithiation) results in a decrease of the carbonate peaks. However, these species appear again in the XPS spectra throughout the delithiation reaction in stage III and they are more pronounced in the case of the LiBOB than LiBOB+VC where a mix of carbonates and ester species are present. The disappearance of the carbonate peaks in LiBOB+VC coincides with the decrease in the ether peaks seen in C 1s and O 1s. The ether (C—O) groups can be part of the carbonates as well as the oxalates and they can also be formed from the decarboxylation reaction of the solvents/additive, which means that they have contributions from all electrolyte components and therefore it is difficult to determine its source. However, the disappearance of carbonates and ethers with LiBOB+VC could suggest that these compounds are connected.[63]

Regarding the Li_2O peak in the O 1s 7.05 keV spectra, its intensity increases until the end of lithiation in stage II and it remains fairly constant afterward during delithiation in stage III for both electrolytes and even clearer for LiBOB. The increase of Li_2O happens concurrently with the disappearance of the carbonate peak in the SEI, which could indicate the decomposition of carbonates forming Li_2O.[61] This growth of Li_2O along the lithiation has been reported previously by Edström and co-workers with $LiPF_6$, but shows a shrinkage of the peak at delithiation, unlike what is seen here with both LiBOB-based electrolytes.[51]

During delithiation in stage III, a decrease in thickness is observed for all three layers in XRR with both electrolytes. By combining these results with depth-resolved XPS measurements, the thickness evolution can be linked to the chemical changes occurring within the layers. According to the XPS analysis, the mechanisms driving the thickness reduction of the SEIs differ between the LiBOB and LiBOB+VC cells. In the LiBOB cell, the thickness decrease is attributed to the decrease of ester groups in the SEI, whereas in the LiBOB+VC cell, it is primarily caused by a decrease in carbonates. Additionally, the lithiated SiO_2/Si layers (L2 and L3) decrease as expected during delithiation and are confirmed with the XPS as the corresponding peaks shift back to higher binding energies. However, full delithiation is not observed as the Si 2p peaks do not shift completely to the initial binding energy and XRR shows a notably lower density at the end of delithiation. These results show that lithium is being trapped in the silicon wafer which could be due to slow kinetics and the cyclic voltammetry experiment not giving enough time for a full lithiation to occur. This has previously been shown for fluorinated systems as well.[52,64,65]

At the end of delithiation, XRR results show that the SEI formed with LiBOB electrolyte is slightly thinner but exhibits higher electron density and roughness compared to LiBOB+VC. XPS results indicate carbonates as the dominant chemical species in the SEI of LiBOB, whereas ester, ether, and carbonate groups are equally distributed in the SEI of LiBOB+VC. The combination of XRR and XPS implies that VC addition leads to a slightly thicker, lower-density, and smoother SEI with more polymeric species combining carbonates, ester, and ether groups.

Upon long-term cycling, after 1, 3, and 10 cycles, a continuous decomposition of the BOB anion is seen in the case of the LiBOB electrolyte (increase in ester peak), with more solvents/additive decomposition seen with LiBOB+VC as the carbonate species increase with cycle number. Furthermore, lithium trapping is observed throughout cycling as seen from the slight shift in Si 2p binding energy compared to the pristine wafer. This could be explained by the use of cyclic voltammetry forcing the potential to change, not allowing the material to reach equilibrium. Nevertheless, lithium trapping is observed with both electrolytes, although to a slightly larger degree for LiBOB.

Overall, these results indicate a SEI breathing behavior and lithium trapping in the silicon wafer for both fluorine-free electrolytes. XRR shows the build-up of the SEI at the end of stage II and a decrease in thickness during stage III. This is consistent with carbonates/esters and SiO_2 disappearing during the SEI build-up phase, and carbonate peaks appearing again in the subsequent stage seen in XPS. The addition of VC provides a thicker and smoother SEI with a slightly different chemical composition throughout the lithiation/delithiation processes, as illustrated in Figure 8. XRR confirms that the silicon wafer (L2) remains in a lithiated state at the end of delithiation, indicative of lithium trapping within the silicon wafer. Meanwhile, L3 is being delithiated to a larger extent, not showing remaining lithium after cycling. Furthermore, XPS analysis of the wafers cycled without additive shows an increase in lithium trapping with an increasing number of cycles. Conversely, the addition of VC in LiBOB+VC electrolyte slightly reduces this phenomenon, as no increase in lithium trapping is observed after the first cycle.

Our investigation reveals distinctions in the formation and evolution of the SEI, as well as the lithiation of SiO_2-terminated Si wafers in LiBOB-based electrolytes compared to $LiPF_6$-based counterparts, reported in literature.[40–42,50] First, SEI formation initiates earlier in LiBOB-based electrolytes, detected in XRR ≈1.3 V, whereas in $LiPF_6$-based systems, inorganic SEI typically forms ≈0.7 V. Furthermore, the literature suggests that the native oxide layer on Si wafers acts as a protective barrier in $LiPF_6$-containing electrolytes, shielding against decomposition of electrolytes prior to lithiation.[42,50] Our study aligns with this notion, as lithiation of SiO_2 in LiBOB-based electrolytes coincides with SEI formation. Concurrently, Li_2O is also formed as SiO_2 is being lithiated, and remains throughout the cycling, while for $LiPF_6$-based electrolytes the formation of Li_2O has been reported to be reversible, disappearing at the delithiated state.[51] Another disparity arises in the lithiation/delithiation behavior of Si wafers

between LiBOB and $LiPF_6$-based electrolytes. In $LiPF_6$ systems – with galvanostatic cycling – Si wafers exhibit a reversible lithiation/delithiation process throughout the cycle.[41,50] However, our XRR results – with cyclic voltammetry and therefore limiting the (de)lithiation reaction – reveal the persistence of a low-density layer beneath the SEI after delithiation in LiBOB-based electrolytes. These differences could be due to the different electrochemical measurements used for cycling or higher SEI resistance with LiBOB-based systems compared to $LiPF_6$.

3. Conclusion

In conclusion, this study offers significant insights into the surface behavior of fluorine-free LiBOB-based electrolytes, with and without the presence of VC as an additive on SiO_2-terminated single-crystalline (001) Si wafer electrodes used as model systems. Through a combination of *operando* XRR and ex situ XPS techniques, we have unraveled the complex processes involved in SEI formation, SiO_2/Si lithiation, and the influence of the VC additive.

Our findings highlight three distinct stages in the SEI evolution during (de)lithiation. Initially, the SEI formation is detected with XRR from 1.3 V, concurrent with the lithiation of the SiO_2 layer and the appearance of Li_2O. The addition of VC is shown to inhibit LiBOB decomposition early on and promote smoother SEI formation. Subsequently, the densification and further growth of the SEI occur alongside continued lithiation of SiO_2 and Si layers. Finally, during delithiation, a decrease in SEI thickness is observed for both electrolytes, indicating a breathing behavior. The comparison of the final SEI layers with different LiBOB-based electrolytes reveals that VC addition leads to a slightly thicker and smoother SEI with lower electron density composed of carbonates mainly. Without VC the layer is a mixture of ester/carbonates/ether species that, suggests continuous decomposition of the BOB anion. Persistent lithium trapping within the Si wafer is observed with the upper layer (L2) remaining lithiated in both LiBOB-based systems post-delithiation, with the phenomenon becoming more pronounced over cycling. Overall, this study provides robust structural and chemical insights into the fundamental processes governing the SEI formation and Si wafer (de)lithiation in LiBOB-based electrolytes. These findings offer important implications for the design and optimization of fluorine-free electrolyte formulations that require better additives to prevent the main salt decomposition, contributing to the development of sustainable and environmentally friendly lithium-ion batteries.

Supporting Information

Supporting Information is available from the Wiley Online Library or from the author.

Acknowledgements

S.T., G.H., and S.L. conceived the study. Z.L., S.T., and G.H. performed the XRR experiments. Z.L. analyzed the data with help from S.T., G.H., and S.L. T.P., A.J.N., and G.H. performed and analyzed the XPS experiments. All authors discussed the correlations between the sets of data and interpreted the results. Z.L. and T.P. wrote the first draft. All authors revised the manuscript. The authors acknowledge the financial support from the ECO2LIB project (European Union H2020 Research and Innovation Program under Grant agreement No 875514), Diamond Light Source for time on Beamline I09 under Proposal SI33024 and European Synchrotron Radiation Facility for time on BM32 Interface beamline under Experiment number A32-2 842. T.P., A.J.N., J.M., and G.H. acknowledge financial support from STandUP for Energy. They also thank Emil Tronde for his help preparing the samples for XPS.

Conflict of Interest

The authors declare no conflict of interest.

Data Availability Statement

The data that support the findings of this study are available from the corresponding author upon reasonable request.

Keywords

fluorine-free electrolyte, lithium-ion battery, Operando X-ray reflectivity, silicon electrode, solid electrolyte interphase, X-ray photoelectron spectroscopy

Received: November 9, 2024
Revised: December 18, 2024
Published online:

[1] C. Wang, Y. S. Meng, K. Xu, *J. Electrochem. Soc.* **2019**, *166*, A5184.
[2] G. Hernández, R. Mogensen, R. Younesi, J. Mindemark, *Batter. Supercaps* **2022**, *5*, 202100373.
[3] A. Bhandari, J. Bhattacharya, *J. Electrochem. Soc.* **2016**, *164*, A106.
[4] C. Xu, G. Hernández, S. Abbrent, L. Kobera, R. Konefal, J. Brus, K. Edstrom, D. Brandell, J. Mindemark, *ACS Appl. Energy Mater.* **2019**, *2*, 4925.
[5] J. C. Hunter, *J. Solid State Chem.* **1981**, *39*, 142.
[6] S. F. Lux, I. T. Lucas, E. Pollak, S. Passerini, M. Winter, R. Kostecki, *Electrochem. Commun.* **2012**, *14*, 47.
[7] A. Rensmo, E. K. Savvidou, I. T. Cousins, X. Hu, S. Schellenberger, J. P. Benskin, *Environ. Sci. Process. Impacts* **2023**, *25*, 1015.
[8] D. L. Thompson, J. M. Hartley, S. M. Lambert, M. Shiref, G. D. J. Harper, E. Kendrick, P. Anderson, K. S. Ryder, L. Gaines, A. P. Abbott, *Green Chem.* **2020**, *22*, 7585.
[9] C. L. Campion, W. Li, B. L. Lucht, *J. Electrochem. Soc.* **2005**, *152*, A2327.
[10] K. Xu, S. Zhang, T. R. Jow, W. Xu, C. A. Angell, *ECS* **2001**, *5*, A26.
[11] K. Xu, U. Lee, S. S. Zhang, T. R. Jow, *J. Electrochem. Soc.* **2004**, *151*, A2106.
[12] K. Xu, S. Zhang, B. A. Poese, T. R. Jow, *ECS* **2002**, *5*, A259.
[13] K. Xu, U. Lee, S. Zhang, J. L. Allen, T. R. Jow, *ECS* **2004**, *7*, A273.
[14] K. Xu, U. Lee, S. Zhang, M. Wood, T. R. Jow, *ECS* **2003**, *6*, A144.
[15] K. Xu, S. S. Zhang, U. Lee, J. L. Allen, T. R. Jow, *J. Power Sources* **2005**, *146*, 79.
[16] G. Hernández, A. J. Naylor, Y.-C. Chien, D. Brandell, J. Mindemark, K. Edström, *ACS Sustainable Chem. Eng.* **2020**, *8*, 10041.
[17] K. Xu, *Chem. Rev.* **2004**, *104*, 4303.
[18] OECD, *OECD Publishing*, Paris, **1992**.
[19] J. Jiang, J. R. Dahn, *ECS* **2003**, *6*, A180.

[20] K. Xu, *J. Electrochem. Soc.* **2008**, *155*, A733.
[21] T. Melin, R. Lundström, E. J. Berg, *J. Phys. Chem. Lett.* **2024**, *15*, 2537.
[22] M. Nie, B. L. Lucht, *J. Electrochem. Soc.* **2014**, *161*, A1001.
[23] Y.-C. Weng, R. Andersson, M.-T. Lee, J. Mindemark, A. Lindblad, M. Hahlin, G. Hernández, *J. Electrochem. Soc.* **2024**, *171*, 060527.
[24] L. Y. Beaulieu, K. W. Eberman, R. L. Turner, L. J. Krause, J. R. Dahn, *ECS* **2001**, *4*, A137.
[25] M. N. Obrovac, L. Christensen, *ECS* **2004**, *7*, A93.
[26] A. Casimir, H. Zhang, O. Ogoke, J. C. Amine, J. Lu, G. Wu, *Nano Energy* **2016**, *27*, 359.
[27] P. Kumar, C. L. Berhaut, D. Zapata Dominguez, E. De Vito, S. Tardif, S. Pouget, S. Lyonnard, P. Jouneau, *Small* **2020**, *16*, 1906812.
[28] Y. Jin, N.-J. H. Kneusels, P. C. M. M. Magusin, G. Kim, E. Castillo-Martínez, L. E. Marbella, R. N. Kerber, D. J. Howe, S. Paul, T. Liu, *J. Am. Chem. Soc.* **2017**, *139*, 14992.
[29] V. Etacheri, O. Haik, Y. Goffer, G. A. Roberts, I. C. Stefan, R. Fasching, D. Aurbach, *Langmuir* **2012**, *28*, 965.
[30] Y. Jin, N.-J. H. Kneusels, L. E. Marbella, E. Castillo-Martínez, P. C. M. M. Magusin, R. S. Weatherup, E. Jónsson, T. Liu, S. Paul, C. P. Grey, *J. Am. Chem. Soc.* **2018**, *140*, 9854.
[31] C. Xu, F. Lindgren, B. Philippe, M. Gorgoi, F. Bjorefors, K. Edstrom, T. Gustafsson, *Chem. Mater.* **2015**, *27*, 2591.
[32] D. Aurbach, K. Gamolsky, B. Markovsky, Y. Gofer, M. Schmidt, U. Heider, *Electrochim. Acta* **2002**, *47*, 1423.
[33] N.-S. Choi, K. H. Yew, H. Kim, S.-S. Kim, W.-U. Choi, *J. Power Sources* **2007**, *172*, 404.
[34] M.-Q. Li, M.-Z. Qu, X.-Y. He, Z.-L. Yu, *J. Electrochem. Soc.* **2009**, *156*, A294.
[35] W. Huang, A. Marcelli, D. Xia, *Adv. Energy Mater.* **2017**, *7*, 1700460.
[36] C. L. Berhaut, D. Z. Dominguez, P. Kumar, P.-H. Jouneau, W. Porcher, D. Aradilla, S. Tardif, S. Pouget, S. Lyonnard, *ACS Nano* **2019**, *13*, 11538.
[37] M. Fehse, A. Iadecola, L. Simonelli, A. Longo, L. Stievano, *Phys. Chem. Chem. Phys.* **2021**, *23*, 23445.
[38] N. R. Geise, R. M. Kasse, J. Nelson Weker, H.-G. Steinrück, M. F. Toney, *Chem. Mater.* **2021**, *33*, 7537.
[39] J. Maibach, J. Rizell, A. Matic, N. Mozhzhukhina, *ACS Mater. Lett.* **2023**, *5*, 2431.
[40] C. Cao, H.-G. Steinrück, B. Shyam, K. H. Stone, M. F. Toney, *Nano Lett.* **2016**, *16*, 7394.
[41] C. Cao, H. Steinrück, B. Shyam, M. F. Toney, *Adv. Mater. Interfaces* **2017**, *4*, 1700771.
[42] C. Cao, I. I. Abate, E. Sivonxay, B. Shyam, C. Jia, B. Moritz, T. P. Devereaux, K. A. Persson, H.-G. Steinrück, M. F. Toney, *Joule* **2019**, *3*, 762.
[43] G. M. Veith, M. Doucet, R. L. Sacci, B. Vacaliuc, J. K. Baldwin, J. F. Browning, *Sci. Rep.* **2017**, *7*, 6326.
[44] S. Kranz, T. Kranz, A. G. Jaegermann, B. Roling, *J. Power Sources* **2019**, *418*, 138.
[45] X. H. Liu, Y. Liu, A. Kushima, S. Zhang, T. Zhu, J. Li, J. Y. Huang, *Adv. Energy Mater.* **2012**, *2*, 722.
[46] J. Li, N. J. Dudney, X. Xiao, Y. T. Cheng, C. Liang, M. W. Verbrugge, *Adv. Energy Mater.* **2015**, *5*, 1401627.
[47] A. L. Michan, G. Divitini, A. J. Pell, M. Leskes, C. Ducati, C. P. Grey, *J. Am. Chem. Soc.* **2016**, *138*, 7918.
[48] F. Jeschull, F. Lindgren, M. J. Lacey, F. Björefors, K. Edström, D. Brandell, *J. Power Sources* **2016**, *325*, 513.
[49] H.-G. Steinrück, A. Schiener, T. Schindler, J. Will, A. Magerl, O. Konovalov, G. Li Destri, O. H. Seeck, M. Mezger, J. Haddad, *ACS Nano* **2014**, *8*, 12676.
[50] C. Cao, B. Shyam, J. Wang, M. F. Toney, H.-G. Steinrück, *Acc. Chem. Res.* **2019**, *52*, 2673.
[51] B. Philippe, R. Dedryvère, J. Allouche, F. Lindgren, M. Gorgoi, H. Rensmo, D. Gonbeau, K. Edström, *Chem. Mater.* **2012**, *24*, 1107.
[52] J. Li, J. R. Dahn, *J. Electrochem. Soc.* **2007**, *154*, A156.
[53] R. I. R. Blyth, H. Buqa, F. P. Netzer, M. G. Ramsey, J. O. Besenhard, P. Golob, M. Winter, *Appl. Surf. Sci.* **2000**, *167*, 99.
[54] N. Schulz, R. Hausbrand, L. Dimesso, W. Jaegermann, *J. Electrochem. Soc.* **2018**, *165*, A819.
[55] A. L. Michan, B. S. Parimalam, M. Leskes, R. N. Kerber, T. Yoon, C. P. Grey, B. L. Lucht, *Chem. Mater.* **2016**, *28*, 8149.
[56] L. El Ouatani, R. Dedryvère, C. Siret, P. Biensan, S. Reynaud, P. Iratçabal, D. Gonbeau, *J. Electrochem. Soc.* **2008**, *156*, A103.
[57] S. Malmgren, K. Ciosek, M. Hahlin, T. Gustafsson, M. Gorgoi, H. Rensmo, K. Edström, *Electrochim. Acta* **2013**, *97*, 23.
[58] S.-P. Kim, A. C. T. Van Duin, V. B. Shenoy, *J. Power Sources* **2011**, *196*, 8590.
[59] B. Philippe, R. Dedryvère, M. Gorgoi, H. Rensmo, D. Gonbeau, K. Edström, *J. Am. Chem. Soc.* **2013**, *135*, 9829.
[60] G. P. López, D. G. Castner, B. D. Ratner, *Surf. Interface Anal.* **1991**, *17*, 267.
[61] E. Peled, D. Golodnitsky, C. Menachem, D. Bar-Tow, *J. Electrochem. Soc.* **1998**, *145*, 3482.
[62] M. Nie, J. Demeaux, B. T. Young, D. R. Heskett, Y. Chen, A. Bose, J. C. Woicik, B. L. Lucht, *J. Electrochem. Soc.* **2015**, *162*, A7008.
[63] N. Gogoi, R. Lundström, G. Hernández, E. J. Berg, *J. Electrochem. Soc.* **2024**, *171*, 050506.
[64] D. Rehnlund, F. Lindgren, S. Böhme, T. Nordh, Y. Zou, J. Pettersson, U. Bexell, M. Boman, K. Edström, L. Nyholm, *Energy Environ. Sci.* **2017**, *10*, 1350.
[65] M. C. Heintz, J. Grins, A. Jaworski, G. Svensson, T. Thersleff, W. R. Brant, R. Lindblad, A. J. Naylor, K. Edström, G. Hernández, *ChemElectroChem* **2023**, *10*, 202300331.